nature biomedical engineering

ARTICLES

https://doi.org/10.1038/s41551-018-0323-x

A wireless and artefact-free 128-channel neuromodulation device for closed-loop stimulation and recording in non-human primates

Andy Zhou[1,5], Samantha R. Santacruz[1,2,5], Benjamin C. Johnson[1,3,5], George Alexandrov[1], Ali Moin[1], Fred L. Burghardt[1], Jan M. Rabaey[1,6], Jose M. Carmena[1,2,6] and Rikky Muller[1,3,4,6*]

Closed-loop neuromodulation systems aim to treat a variety of neurological conditions by delivering and adjusting therapeutic electrical stimulation in response to a patient's neural state, recorded in real time. Existing systems are limited by low channel counts, lack of algorithmic flexibility, and the distortion of recorded signals by large and persistent stimulation artefacts. Here, we describe an artefact-free wireless neuromodulation device that enables research applications requiring high-throughput data streaming, low-latency biosignal processing, and simultaneous sensing and stimulation. The device is a miniaturized neural interface capable of closed-loop recording and stimulation on 128 channels, with on-board processing to fully cancel stimulation artefacts. In addition, it can detect neural biomarkers and automatically adjust stimulation parameters in closed-loop mode. In a behaving non-human primate, the device enabled long-term recordings of local field potentials and the real-time cancellation of stimulation artefacts, as well as closed-loop stimulation to disrupt movement preparatory activity during a delayed-reach task. The neuromodulation device may help advance neuroscientific discovery and preclinical investigations of stimulation-based therapeutic interventions.

Closed-loop neuromodulation improves open-loop therapeutic electrical stimulation by providing adaptive, on-demand therapy, reducing side effects and extending battery life in wireless devices[1,2]. Closing the loop requires low-latency extraction and accurate estimation of neural biomarkers[3–5] from recorded signals to automatically adjust when and how to administer stimulation as feedback to the brain. Recent studies have shown responsive stimulation to be a viable option for treating epilepsy[2,6], and there is evidence that closed-loop strategies could improve deep brain stimulation (DBS) for treating Parkinson's disease and other motor disorders[7,8]. However, there is presently no commercial device allowing closed-loop stimulation for DBS in patients with movement disorders, and strategies for implementing such stimulation are still under investigation. In fact, most attempts to close the loop for DBS treatments have been done only for short duration using systems that were not fully implantable[4,5,9–11]. To enable advanced research in closed-loop neuromodulation, there is a need for a flexible research platform, for testing and implementing these various closed-loop paradigms, that is also wireless, compact, robust and safe.

Designing such a device requires unification of multi-channel recording, biomarker detection and microstimulation technologies into a single unit with careful consideration of their interactions. Wireless, multi-channel recording-only devices capture activity from wide neuronal populations[12,13], but do not have the built-in ability to immediately act on that information and deliver stimulation. Several complete closed-loop devices have been proposed and demonstrated, but are limited by low channel counts[14–17] and low wireless streaming bandwidth[14–18]. Most recently, variations of the fully integrated and optimized closed-loop neuromodulation system-on-a-chip (SoC) have been presented, but full system functionality has not yet been adequately demonstrated in vivo[19–25]. While future versions may be paired with miniaturized external battery packs and controllers, current systems built around these SoCs require large, stationary devices to deliver power inductively from a close range[19,21,23]. This limits studies to using small, caged animals.

Furthermore, any device for concurrent sensing and stimulation must be able to mitigate or remove stimulation artefacts—the large voltage transients resulting from stimulation that distort recorded signals and obscure neural biomarkers. Signals recorded concurrently with stimulation may contain relevant information for closed-loop algorithms or offline analysis, yet existing devices disregard these affected windows of data, or fail to reduce artefacts to an acceptable level for recovery of many potentially useful biomarker features. Effectively and efficiently cancelling artefacts requires careful co-design of the stimulators and signal acquisition chains. Additionally, computational reprogrammability is needed for application-dependent algorithm design in both artefact cancellation and closed-loop control.

The wireless artefact-free neuromodulation device (WAND) introduced here incorporates all the key features needed to continuously monitor neural biomarkers in the presence of stimulation artefacts and deliver closed-loop stimulation. WAND combines: (1) 2 custom-designed, 64-channel neural interface application-specific integrated circuits supporting simultaneous low-noise recording and high-current stimulation, specifically designed to minimize stimulation artefacts; (2) flexible and reprogrammable back-end processing on a SoC field-programmable gate array (FPGA) for cancelling residual artefacts, computing neural biomarkers, running closed-loop algorithms and controlling stimulation; and (3) a robust, bidirectional wireless link to a graphical user interface (GUI)

[1]Department of Electrical Engineering and Computer Sciences, University of California, Berkeley, Berkeley, CA, USA. [2]Helen Wills Neuroscience Institute, University of California, Berkeley, Berkeley, CA, USA. [3]Cortera Neurotechnologies, Inc., Berkeley, CA, USA. [4]Chan Zuckerberg Biohub, San Francisco, CA, USA. [5]These authors contributed equally: Andy Zhou, Samantha R. Santacruz, Benjamin C. Johnson. [6]These authors jointly supervised this work: Jan M. Rabaey, Jose M. Carmena, Rikky Muller. *e-mail: rikky@berkeley.edu

for device configuration and control, as well as data logging. These features are tightly integrated into a small form factor, low-power device, enabling many proposed closed-loop and responsive neuromodulation applications, as well as offering a platform for developing new ones. To demonstrate the various functions of WAND, we performed a series of in vivo experiments that validate long-term, high-fidelity and wireless multi-channel recording; real-time, complete removal of stimulation artefacts for accurate recovery of neural signals; and on-board biomarker detection for closed-loop control.

System design

WAND is designed to be a general-purpose tool with immediate applicability in various research environments. Inclusion of a wide feature set is balanced by limitations in device size and power.

Integrated circuits are required to minimize area and power for a large number of recording and stimulation channels. We custom-designed a neuromodulation integrated circuit (NMIC) to deliver stimulation pulses ranging from subthreshold currents (down to 20 µA) to those required by DBS (5 mA), and to record local field potentials (LFPs) with a bandwidth of up to 500 Hz[26]. We chose LFPs as the signals of interest for their usefulness in medical applications as an indicator of disease[8,27–30]. There is also evidence that LFPs can be used for motor decoding in brain–machine interfaces[31–35], with comparable accuracy and better longevity than spike decoders[35]. This signal is also extremely useful to understanding neural processing, and is incredibly relevant for a variety of basic neuroscience studies, from investigating how neural oscillations coordinate movement[36–38] to cued transitions between dynamic states in corticobasal ganglia circuits[39] and working memory[40,41]. Finally, the lower (1 kHz) sampling rate required for LFP recording utilizes a lower wireless bandwidth for real-time streaming, allowing the use of low-power, off-the-shelf radios.

While numerous high-channel-count recording circuits have been designed[42,43], state-of-the-art circuits cannot tolerate—and often exacerbate—the effects of stimulation artefacts. Electrical stimulation generates a large voltage transient (direct artefact), concomitant with stimulation current and charge delivery to neural tissue and nearby electrodes. The direct artefact may be many orders of magnitude larger that the underlying neural signal (mV compared with µV, respectively). This is followed by a long, post-stimulus voltage decay (indirect artefact) determined by the mismatch of stimulation phases and electrode properties. Conventional low-noise, low-power neural amplifiers are sensitive to both direct and indirect artefacts, saturating from both[44,45]. They recover slowly from saturation due to long time constants of analogue feedback, causing data loss during—and many milliseconds after—a stimulation pulse. State-of-the-art methods for mitigating the indirect artefact try to prevent saturation of the front ends. Saturation can be prevented by increasing the amplifier linear input range and tolerance to d.c. current offset[21,26,46], or by subtracting the large amplitude components of the artefact[47,48]. Artefact duration can be reduced by rapidly clearing charge built up on circuit elements from stimulation[25,26,49,50]. We have designed the NMICs with improved stimulation and recording architectures to both prevent large indirect artefacts and minimize their effects on the front-end circuits.

To date, even the best results in front-end artefact mitigation do not demonstrate complete artefact removal, necessitating back-end digital cancellation for residual artefacts. Computationally efficient back-end methods include subtractive methods (where artefact templates are subtracted from the waveform to reveal the underlying signal[48,51,52]) and reconstructive methods (where segments of corrupted data are replaced with interpolated values[53–55]). Different techniques may achieve better results than others, depending on the level of mitigation achieved by the front-end amplifiers.

Overall system resiliency to stimulation artefacts depends heavily on the co-design of the stimulator, signal processing blocks and recording front end. In this work, we demonstrate how the specific artefact prevention and mitigation techniques utilized in the NMICs motivate our implementation of back-end linear interpolation in an on-board SoC FPGA to completely remove stimulation artefacts in real time. In particular, the reduced artefact duration allows for a computationally inexpensive but effective back-end cancellation solution at the cost of losing only one or two samples. These innovations allow for online, real-time biomarker computation for closed-loop stimulation.

Results

WAND architecture. WAND components and architecture are shown in Fig. 1. For this work, the form factor was designed to fit into the polyetherimide housing for a custom-built chronically implanted microelectrode array (Gray Matter Research). The device has a board area of 10.13 cm^2 and weighs 17.95 g together with a rechargeable 500 mAh lithium-ion battery pack, allowing 11.3 h of continuous, wireless operation (Fig. 1a). The main components of WAND are the pair of custom-designed NMICs, a SoC FPGA, a radio SoC and support circuitry for power regulation and programming (Fig. 1b–d).

Each NMIC consists of 64 recording channels and 4 stimulators that can address any of the 64 channels, meaning that stimulation can occur simultaneously on up to 8 channels by leveraging stimulators across the 2 on-board NMICs. Multi-site stimulation is desirable for implementing specific spatiotemporal patterns of stimulation, with many recent studies performing stimulation on two to eight channels simultaneously[56–61]. Using WAND, the stimulation channels can be dynamically assigned, thus allowing this device to be utilized for multi-site stimulation on up to eight channels concurrently in a highly flexible manner. Ultimately, stimulation can be delivered using an open-loop paradigm or a closed-loop approach that relies on continuous sensing of on-board computed biomarkers.

Stimulation parameters are rapidly reprogrammable by writing to registers on the NMIC through commands transmitted from a GUI, or automatically based on calculations performed on board. All stimulation settings listed in Supplementary Fig. 1, as well as the selection of stimulation sites and triggering of pulses, can be set through the same interface. A new setting can be preloaded while stimulating with a previous setting, potentially reducing latency between biomarker state detection and the resulting stimulation update.

Unlike conventional neural interface integrated circuits, the NMICs enable simultaneous low-noise, low-power neural recording of LFP with high-compliance electrical stimulation (Fig. 1c). The NMIC prevents large amplitude indirect artefacts by employing stimulators with highly accurate charge balancing[26]. Accurate charge balancing is achieved by reusing the same current source for both phases of a biphasic pulse and a return-to-ground stimulator architecture (Supplementary Fig. 2 and the section 'System artefact resiliency' in the Supplementary Information). To address both direct and indirect artefacts, the NMIC recording front ends are designed simultaneously for low-noise (1.6 μV_{rms} (root-mean-square voltage) mean channel noise) recording and a large linear input range of 100 mV. The input range is over ten times larger than conventional designs[42,43] and avoids saturation in the presence of large stimulation artefacts (tens of mV) while still being able to resolve µV-level neural signals. This large range of resolvable signals is achieved with a mixed-signal architecture that integrates the analogue-to-digital converter (ADC) into the feedback loop, thereby reducing the required gain and signal swings. The architecture also resets at every sample, enabling memoryless sampling and rapid recovery from stimulation artefacts (Supplementary Fig. 4). Therefore, stimulation artefacts do not persist beyond the samples when stimulation is occurring, and minimal data are lost when using reconstructive back-end cancellation methods such as interpolation.

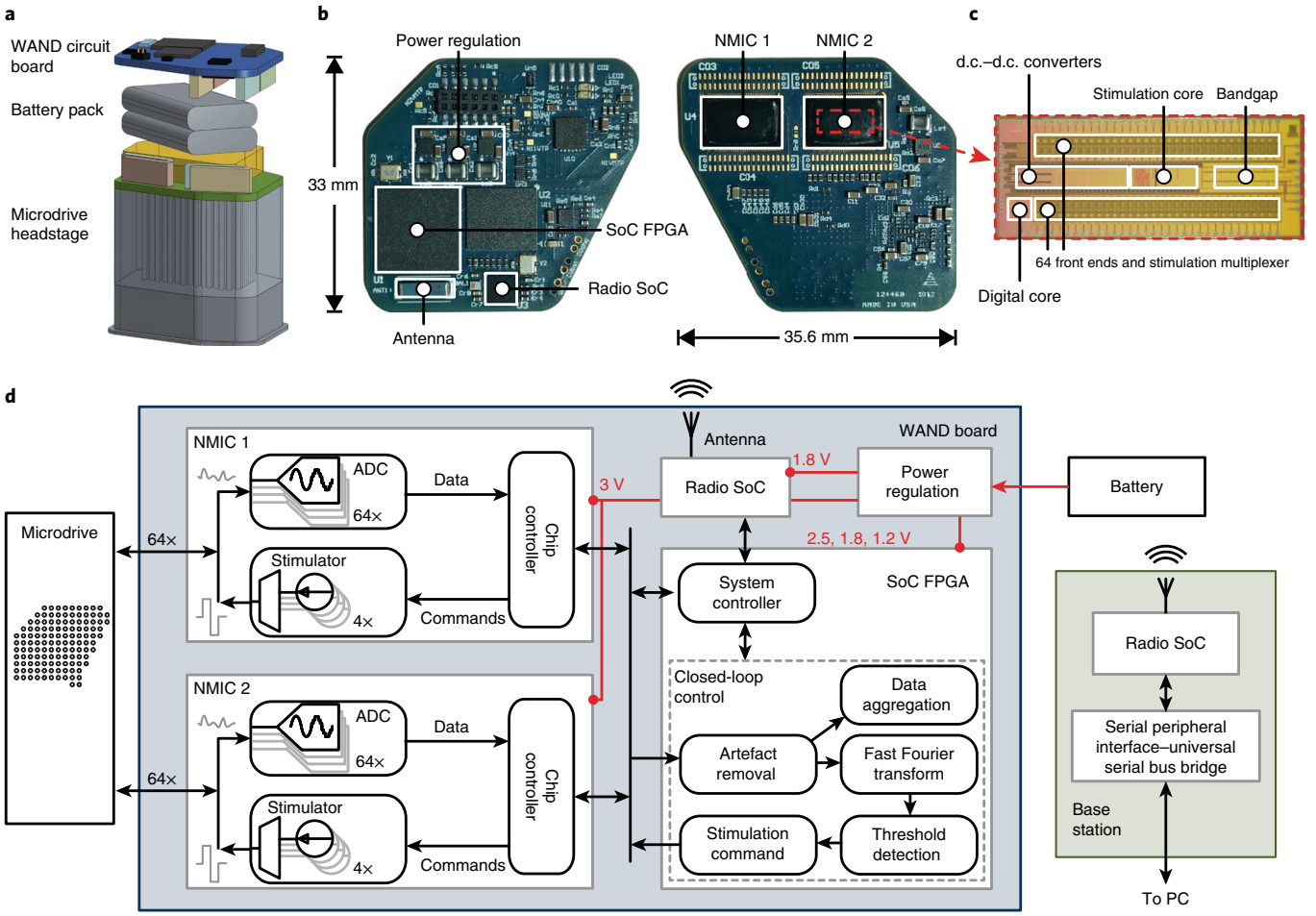

Fig. 1 | WAND system architecture. a, Three-dimensional computer-aided design model of WAND with a primate headstage and battery pack, shown without the polyetherimide case. **b**, Top- (left) and bottom-view (right) photographs of the WAND circuit board, showing its relevant subsystems and dimensions (33 mm (H) × 35.6 mm (W)). **c**, Micrograph of an NMIC with annotated subcircuits. **d**, Functional diagram of the WAND system, showing data and power connections on the main device board, and connections to the microdrive electrode array, battery and a wireless base station.

All 128 channels of neural data from both NMICs are sampled, digitized (15 bits; 1 kS s^{-1}) and serialized on chip, then transmitted to the on-board FPGA and microcontroller SoC via a custom-designed bidirectional interface implemented in the FPGA fabric[62]. The same interface is used for downlink commands to control NMIC circuitry and update stimulation parameters (Fig. 1d). Software running on the included Cortex-M3 microprocessor then aggregates neural and other sensor data, cancels stimulation artefacts, selects a subset of data to be streamed back to the base station and runs closed-loop neuromodulation algorithms (Fig. 1d). The FPGA fabric and Cortex-M3 software are reprogrammable through a serial wire debug interface, allowing customization for different applications. A 2.4 GHz Bluetooth Low Energy (BLE) radio SoC allows for robust bidirectional wireless communication up to 2 m from the subject. BLE offers low-power telemetry, and customization of the BLE protocol enables data streaming rates close to the 2 Mbp modulation rate. WAND can stream up to 96 uncompressed LFP recording channels in real time to a personal computer (PC) running a custom-built GUI for system configuration and data visualization.

High-fidelity multi-channel wireless recording. To evaluate the quality of recordings made using WAND, we recorded 96 channels of LFP activity from a non-human primate (NHP) using a chronically implanted microdrive electrode array with access to both cortical and subcortical nuclei (Fig. 2a). We compared WAND recordings with sequentially recorded neural data from a wired, state-of-the-art, commercial neurophysiology system (Tucker-Davis Technologies). Respective recordings from each system have qualitatively similar signal properties, as assessed by computing the power spectral densities of the recorded data (Fig. 2b,c). The WAND recordings exhibit lower 60 Hz interference due to the lack of long interface cables and better-isolated recording references.

To demonstrate robust detection of biomarkers in WAND recordings and establish a baseline for neuromodulation experiments, we recorded LFP activity during a standard self-paced, centre-out joystick task (Fig. 3a,b). During this behaviour, ongoing beta and high-gamma rhythms are inversely modulated by task-related periods of movement (Fig. 3c,d). Beta band oscillations are found to emerge during specific motor actions and notably before instructed reaches or movements[37,63,64]. In premotor and motor areas, this rhythm has been linked to neural activity related to motor preparation[65–68]. The subject had an average reaction time of 183.3 ± 4.8 (s.e.m.) ms across 400 trials. For LFP signals recorded from premotor and motor areas, we found that the reaction time was significantly correlated with the average power of beta band activity around the go cue (see Methods; Pearson's correlation coefficient, $r = 0.12$; $P = 0.03$).

To validate long-term, wireless system functionality, we performed unconstrained, overnight recordings for five nights in the subject's home cage, recharging the battery between each session

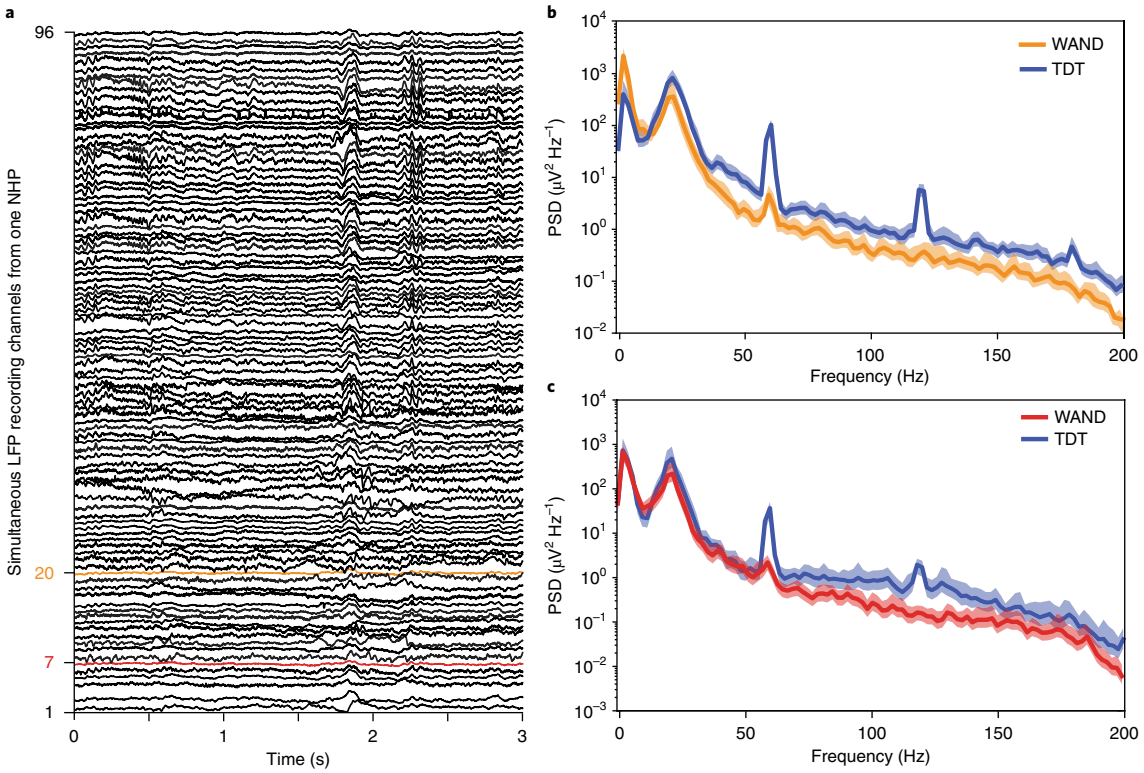

Fig. 2 | Wireless, multi-channel recording. a, Representative 3 s segments of 96 channels of simultaneous LFP recordings taken from one NHP during freely moving behaviour. **b**,**c**, Comparison of mean power spectral densities (PSD) (Welch's method, $n = 1{,}170$ windows, one 5 min recording, 512 ms windows, 256 ms overlap) from channels 20 (**b**) and 7 (**c**) for recordings taken from WAND and subsequent recordings taken from a commercial wired neurophysiology system (Tucker-Davis Technologies (TDT)). Lines represent means, while shaded areas represent s.d.

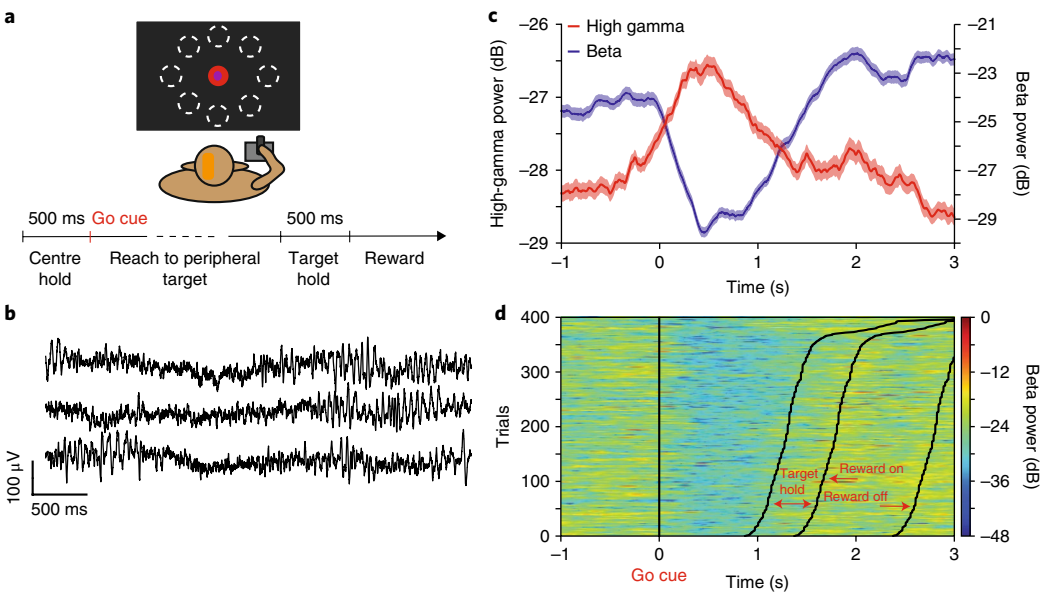

Fig. 3 | LFP recordings during the joystick task. a, Diagram of the centre-out joystick task with a timeline of the task periods for movement and reward. The orange patch on the NHP's head represents the location of the WAND device and headstage implant. **b**, Representative LFP recordings from three channels during the centre-out task. **c**, Trial-averaged ($n = 400$) beta (13–22 Hz) and high-gamma (70–200 Hz) power aligned to the go cue during the centre-out task. Lines represent means, while shaded areas represent s.e.m. **d**, Beta power aligned to the go cue. Each row represents activity from a single trial. Trials are organized by the time to target hold following the go cue.

(Fig. 4a). We recorded on average of 10.2 consecutive hours per night, with a mean packet error rate below 0.5% and a median packet error rate below 0.1%, where each transmitted wireless packet contained 1 ms of neural data from all streamed channels. Offline analysis of the data revealed useful sleep-related biomarkers. Delta (0–4 Hz; Fig. 4b) and theta (4–7 Hz; Fig. 4c) frequency bands are

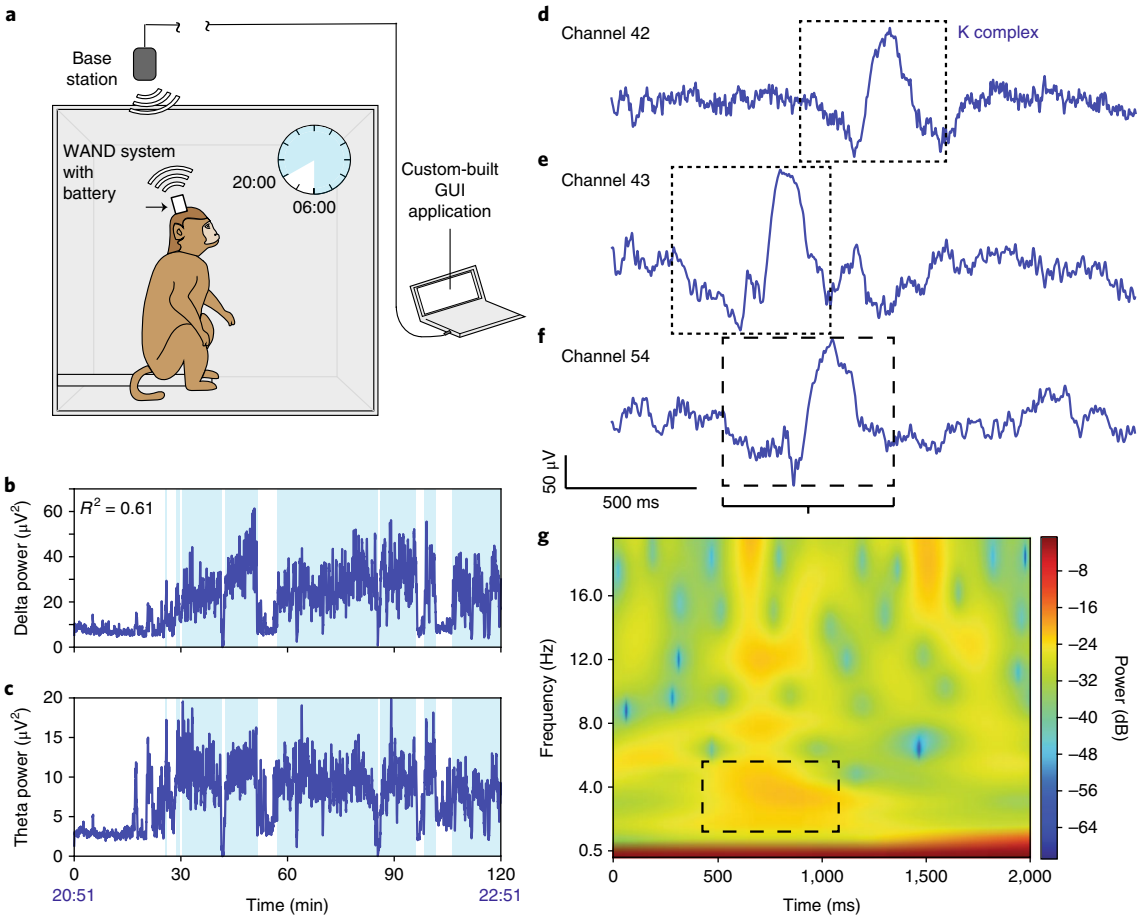

Fig. 4 | Overnight, untethered recording of brain signals from an NHP during sleep. a, Schematic of in-cage wireless recordings. **b**,**c**, Delta (0.5–4 Hz) (**b**) and theta (4–7 Hz) (**c**) power from a 2 h segment of overnight recording beginning at 20:51. The powers are significantly correlated, as shown inset in **b** (squared Pearson's correlation coefficient, $R^2 = 0.61$; $P < 0.001$). K-means clustering was used to classify the activity into states of increased (light blue background) and decreased (white background) delta and theta activity ($n = 14{,}061$ observations, 1,024 ms windows, 512 ms overlap). **d**–**f**, Example K complexes from the caudate (**d** and **e**) and anterior cingulate cortex (**f**). **g**, Spectrogram of activity from channel 54 during the same time window as the waveform shown in **f**. Increased delta power occurs coincidently with the K complex.

known to have elevated power during sleep states relative to wake states[69,70]. K complexes are sleep-specific phasic waveforms that occur spontaneously and are observed through the obtained neural recordings during epochs of increased delta power (Fig. 4d–g), consistent with the classification of sleep-state intervals.

Simultaneous recording and stimulation. True simultaneous recording and stimulation is enabled through co-design of the NMIC artefact prevention and mitigation methods with back-end cancellation algorithms running on the on-board microcontroller. To demonstrate WAND's ability to recover neural signals from stimulation artefacts in real time, we performed experiments delivering open-loop stimulation while recording LFP. For each set of stimulation parameters, we recorded three consecutive segments of LFP: (1) without stimulation; (2) with stimulation turned on, but without back-end artefact cancellation; and (3) with artefact cancellation turned on (Fig. 5a). During the train of identical bipolar, biphasic stimulation pulses, the segment of LFP with uncancelled artefacts (Fig. 5a, middle section) demonstrated varying artefact morphology due to the non-integer ratio between the sampling rate and the stimulation frequency (99.8482 Hz shown) (Fig. 5b). Stimulation pulses occurring completely within a single-sample integration window caused only a single-sample direct artefact, while pulses occurring at the boundary between two integration windows caused the direct artefact to last two samples. We calculated averaged templates of single- and double-sample artefacts (Fig. 5c) for varying stimulation amplitudes and pulse widths, and confirmed a linear relationship between these parameters and the artefact amplitude (Fig. 5d). For all stimulation parameters within our protocol, recorded direct artefacts on the non-stimulating electrodes remained well within the 100 mV linear input range of the front-end amplifiers, despite the high voltages (~10 V) induced on the stimulating electrodes, thus demonstrating saturation-free recording in the presence of stimulation.

Following both single- and double-sample direct artefacts, the indirect artefacts were very small and brief, visible only in the averaged templates (Fig. 5c, inset). Following a single-sample direct artefact, the indirect artefact was already suppressed to within −60 dB of the peak amplitude by the following sample, and to within the electronic noise floor of 1.6 μV_{rms} by the second sample. Indirect artefacts following double-sample direct artefacts were fully suppressed below the noise floor. These results demonstrate that the recording front ends rapidly recovered from stimulation pulses, minimizing data distortion.

Although the recorded artefacts were short in duration and remained in the linear range of the amplifiers, they still caused broadband contamination of the recorded spectrum. We quantified

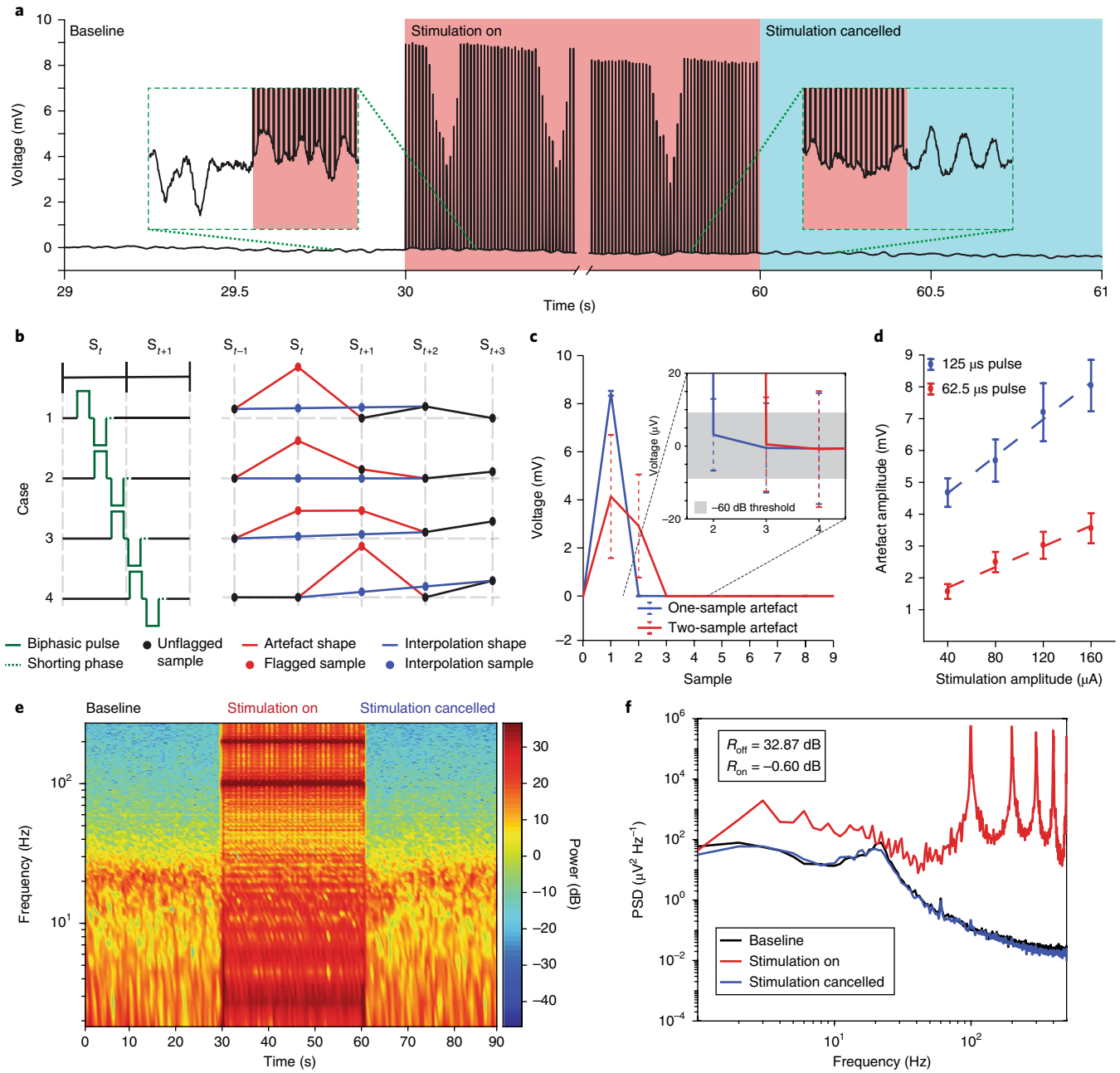

Fig. 5 | Residual artefact analysis and cancellation. a, One second segments of raw signals recorded during different epochs of the open-loop stimulation experiment: baseline LFP with no stimulation (white); stimulation with no artefact cancellation (red); and stimulation with artefact cancellation (blue). Insets: plots show magnified 0.4 s segments of the LFP during transitions from no stimulation to stimulation without artefact cancellation (left), and from stimulation without artefact cancellation to stimulation with artefact cancellation (right). In this example, biphasic pulses were delivered at 100 Hz with 160 µA amplitude and 125 µs pulse widths per phase. **b**, Different cases of relative phases between the stimulation pulse and sampling periods for samples S_t at time t (left), with example resulting samples $S_{t'}$, artefact flags and cancelled samples using linear interpolation (right). **c**, Averaged templates of single-sample (blue) and double-sample (red) flagged artefacts. Inset: magnified portion showing decay of artefacts to within −60 dB of the artefact peak (shaded grey). Error bars show s.d. (n = 2,106 for single-flag and n = 897 for double-flag). **d**, Average amplitude of artefacts from stimulation amplitudes of between 40 and 160 µA and pulse widths of 125 µs (blue) and 62.5 µs (red). Error bars show s.d. (n = 3,003 artefacts). **e**, Spectrogram of the full 90 s recording during the different stimulation epochs for the example in **a**. **f**, Welch's power spectral density (PSD) estimates for each 30 s epoch for the example in **a**. A measure, R (R_{off} without artefact cancellation and R_{on} with cancellation), was calculated as the ratio of signal power integrated from 1–200 Hz of LFP during stimulation to baseline LFP.

this contamination with the ratio R = 32.78 dB, of signal power integrated form 1–200 Hz of LFP during stimulation to baseline LFP (Fig. 5e,f). Since the recorded artefacts are short in duration (one to two samples), we chose to implement a method of linear interpolation for artefact cancellation in the back end[53]. Samples coinciding with stimulation pulses are flagged by the NMIC, ensuring accurate detection of artefacts. Samples were then buffered in the microcontroller, and artefacts were removed by linearly interpolating between the pre-artefact sample and the sample following the maximum possible direct artefact duration (Fig. 5b).

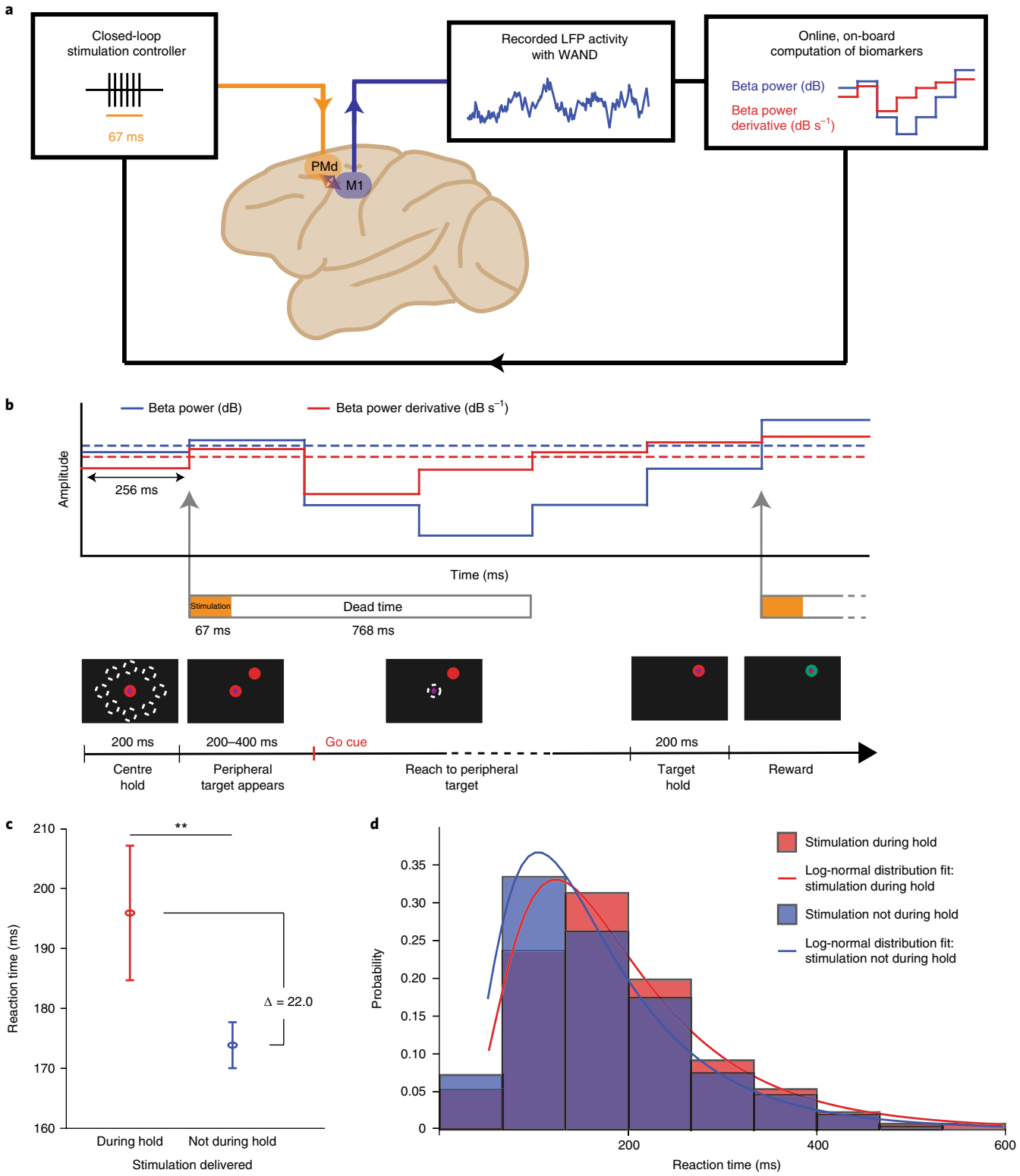

Fig. 6 | In vivo closed-loop experiment to disrupt movement preparatory activity during a delayed-reach task. a, Description of the closed-loop paradigm, where recorded activity in M1 was used to control stimulation in PMd. **b**, Diagram of the delayed-reach task and closed-loop algorithm implemented during this task. Stimulation was delivered when the beta power and its derivative exceed their thresholds. **c**, Mean reaction times for trials ($n = 997$) in which stimulation was delivered successfully during the hold period compared with when it was not. Error bars represent s.e.m. Significance was determined using a two-sided Mann-Whitney U-test ($U = 44{,}193.5$, $n_1 = 131$ group size of stimulation delivered during hold, $n_2 = 763$ group size of stimulation not delivered during hold; $^{**}P = 0.003$). **d**, Normalized reaction-time histograms and log-normal fits to approximate the respective probability density functions ($n = 997$ independent experiments).

Table 1 | Comparison of closed-loop neuromodulation systems with full in vivo validation

	Neurochip-2[15]	PennBMBI[16]	University of Toronto[18,44,73]	NeuroPace RNS[17,74,75]	Activa PC + S[14,71,72,76]	WAND (this work)
Dimensions	63 × 63 × 30 mm^3	56 × 36 × 13 mm^3 neural signal analyser unit; 43 × 27 × 8 mm^3 stimulator unit	22 × 30 × 15 mm^3	28 × 60 × 7.7 mm^3	39 cm^3	36 × 33 × 15 mm^3
Weight	36 (39[a]) g boards; 145 (204[a]) g total	–	12 g total	16 g	67 g total	7.4 g board; 17.95 g total
Power	284–420 mW	290 mW[b]	45 mW	–	–	172 mW
Wireless link	IR	Nordic Enhanced Shockburst	ZigBee	20–50 kHz short-range inductive	175 kHz ISM	Nordic BLE
Data rate	–	2 Mbps	250 kbps	–	11.7 kbps	1.96 Mbps
Real-time streaming	No	4 channels	1 channel[b]	1 channel	2 channels raw; 4 channels compressed	96 channels + 3 accelerometer channels
Number of recording channels	3	4	256	4	4	128
Recording power per channel	–	1.25 mW channel^{-1}	52 μW channel^{-1}	–	5 μW channel^{-1}	8 μW channel^{-1}
Sampling rate	2/24 kS s^{-1} (24 kS s^{-1} only on one channel)	21 kS s^{-1}	15 kS s^{-1}	250 S s^{-1}	422 S s^{-1}	1 kS s^{-1}
ADC resolution	8 bits	12 bits	8 bits	10 bits	10 bits	15 bits
Artefact mitigation	Transient gain reduction	None	None	Low-pass filter	Front-end filtering; heterodyning; symmetric sensing	DR increase; memoryless sampling
Number of stimulation channels	3	2	64	8	8	128
Maximum current	5 mA	1 mA	250 μA	11.5 mA	25.5 mA	5 mA
Compliance	±15 (50[a]) V	±12 V	2.6 V	12 V	±10 V	12 V
Charge balancing	Matching resistors (0.1%)	0.75% mismatch	–	<10 μC s^{-1} charge imbalance	Passive discharge	Biphasic current source reuse; 0.016% mismatch
Artefact cancellation	No	No	No	No	Stimulation as feature for SVM	Linear interpolation
Biomarker detection	Spectral power; action potential detection	Spectral power; time domain features; action potential detection	Phase locking value seizure precursor	ECoG signal intensity; line length; half-wave	Spectral power	Spectral power
Closed-loop control	Detection/ threshold triggered	Detection/threshold/ sensor triggered	Thresholding	Detection/ thresholding	Two-dimensional SVM	Thresholding
Animal model	Primate	Rodent	Rodent	Human	Ovine	Primate
In vivo closed-loop paradigm	Spike triggered	Sensor-node event (button press) triggered	Phase locking value threshold triggered	Seizure detection and responsive treatment	SVM classification (spectral power; stimulation) triggered	Spectral power threshold triggered

[a]High-compliance stimulation version. [b]Estimated. IR, infrared; DR, dynamic range; BLE, bluetooth low energy; SVM, support vector machine; ECoG, electrocorticography.

While more sophisticated techniques may be employed, we found that this simple linear interpolation was sufficient to suppress the artefact power below the neural signal spectrum. Interpolation over two samples at 100 Hz in baseline LFP data without stimulation caused no significant degradation of the spectrum ($R = 0.0091$ dB). Furthermore, this method did not depend on the actual values of the artefacts and was not affected by the varying artefact morphology, which would have complicated and increased convergence times of template subtraction and adaptive filtering techniques. With on-board artefact cancellation enabled, we were able to recover the baseline LFP spectrum for signals recorded during the simulation pulse train with $R = -0.60$ dB (Fig. 5a–f).

In vivo biomarker extraction and closed-loop experiment. To further demonstrate WAND's ability to mitigate stimulation artefacts in real time, and to perform responsive stimulation using on-board computations, we designed a closed-loop stimulation experiment to disrupt movement preparatory activity during a delayed-reach task (Fig. 6a). Previous work in macaque monkeys has shown that microstimulation delivered to dorsal premotor (PMd) and primary motor (M1) cortical sites during the delay hold period of a delayed-reach

task disrupts preparatory activity and causes an increase in the reaction time[67]. In the study, stimulation was timed synchronous to the task and was not triggered on recorded neural activity. We reproduced this result by detecting periods of preparation (holding) before movement using recorded neural activity in M1 and delivering stimulation to electrodes in PMd in response. In this way, stimulation was automatically controlled by WAND, running in a closed-loop manner relying solely on neural activity and completely separate from the task.

Beta-band activity (13–30 Hz) is known to reflect movement states, with lower beta-band power associated with periods of movement and higher beta-band power associated with the absence of movement. Thus, we chose beta-band power as the WAND control signal for closed-loop classification of hold periods before movement. In this way, closed-loop operation of WAND was completely agnostic to the behaviour task states, and stimulation delivery relied solely on the control signal. We heuristically selected a policy of delivering a preconfigured stimulation pulse train when both the beta power and its derivative exceeded programmed thresholds during the delayed-reach task (Fig. 6b). The pulse train parameters were selected to closely match values used in previous work (333 Hz for 57 ms)[67] within WAND specifications. To avoid stimulation multiple times within the same delay hold period, our policy also incorporated a 'dead time' of three calculation periods, or 768 ms. Neural activity was recorded throughout the task, and while stimulation turn-off can be based on neural signature, we chose to adhere to the durations used in previous work to demonstrate reproducibility of an established result.

Post-hoc analysis showed that reaction times increased significantly in behavioural trials when stimulation was delivered during the hold period before the go cue, relative to trials when it was not (Fig. 6c). The increase of 22.0 ms in average reaction time, consistent with previously reported results for microstimulation delivered in PMd, and the change in the reaction time distribution (Fig. 6d) indicate that neural preparatory activity was successfully disrupted using our closed-loop neuromodulation approach. This functional change in behaviour serves as a representative demonstration of how WAND may be used to compute biomarkers in real time as part of a closed-loop stimulation paradigm and perform online stimulation artefact mitigation.

Discussion

We have demonstrated WAND—a small form factor, wireless neuromodulation device enabling simultaneous recording and stimulation for a variety of research purposes. Integration of a custom-designed application-specific integrated circuit with an on-board FGPA and radio enables high-quality, long-term multichannel recording and stimulation during free behaviour, full cancellation of stimulation artefacts, flexible programmability and low-latency processing for delivery of closed-loop microstimulation based on detected biomarkers.

Table 1 summarizes the WAND system specifications and compares them with those of other recently published closed-loop neural interfaces that have been fully packaged and validated in vivo. We view WAND as a deployable research tool ready for use with large animals, and potentially humans, and we therefore limit our comparisons to similar devices that can operate fully wirelessly and autonomously to have an immediate impact on scientific and clinical discovery; however, a comparison of neural interface integrated circuits is also presented in Supplementary Table 1. Our criteria include: fully on-board recording, computation and stimulation ability; wireless data streaming or on-board memory for data storage; and an implantable or wearable power source. The Neurochip-2[15], PennBMBI[16], NeuroPace RNS[17] and Activa PC+S[14,71,72] devices allow for flexible biomarker detection and triggered stimulation, but with a low number of channels. A device developed at the University of Toronto[18,44,73] enables recording and stimulation on more channels, but all of these devices still stream data at a low rate, preventing large-scale multi-site analysis. WAND improves on these limitations by incorporating a large number of recording and stimulation channels, a wireless data rate to support a large number of streaming channels, and closed-loop neuromodulation capabilities. It also actively cancels stimulation artefacts through both hardware and software techniques for completely artefact-free recording during stimulation. Although the Neurochip-2 and Activa PC+S devices utilize some hardware and experimental setup techniques, large residual artefacts still appear to affect performance during stimulation[14,15].

The experiments shown here are intended to outline and demonstrate the capabilities enabled by WAND, paving a path towards the use of this technology as a tool in clinical and neuroscientific research. For this work, device form factor, size, channel count and sensor integration were designed specifically to interface with the microelectrode array implanted in the primate subject. Future research will incorporate other features of WAND, such as the inertial sensor and multi-site stimulation. The architecture of WAND makes it amenable to function as a general-purpose research device, requiring only minor modifications to be re-optimized for new applications. Algorithmic development on the FPGA and microcontroller allows for extracting other neural biomarkers, such as band powers or line lengths used to detect seizure onset in epileptic patients[3], and new closed-loop classification and control algorithms may be conceived for integrating neural activity from a larger number of recording channels. Further research in electrode configuration and improved backend artefact cancellation algorithms may allow recovery of the full underlying neural signal with no lost samples—a limitation WAND still faces. Currently, the closed-loop control and artefact cancellation algorithms are implemented in the microcontroller, with very little of the FPGA fabric resource (<5%) being utilized. Preliminary results of porting these algorithms to the fabric indicate that there is still ample room for increasing their complexity to achieve better efficacy.

In a clinical context, the device can be hermetically packaged and used to provide on-demand therapy in deep-brain stimulation while continuously monitoring the neurological response during treatment. For example, in Parkinson's disease patients treated with DBS, a spectral peak biomarker linked to dyskinesia (an adverse effect of DBS therapy) has been discovered[8]. The closed-loop paradigm we demonstrate in this work can be easily modified for this application, as our current biomarker detection algorithm can already be used to sense this spectral peak. Modifying the control policy to reduce stimulation amplitude, rather than trigger stimulation when the peak is detected, can thereby reduce the incidence of this undesirable side effect.

Methods

WAND board components. The WAND board (Fig. 1b–d) consists of a SoC FPGA with a 166 MHz Advanced RISC Machine (ARM, where RISC stands for reduced instruction set computer) Cortex-M3 processor (SmartFusion2 M2S060T; Microsemi) acting as a master module. The FPGA forms a custom-designed 2 Mb s^{-1} digital signal and clock interface with a pair of NMICs, aggregating data and commands in hardware first-in first-out memories[62]. The Cortex-M3 processor selects which channels are streamed or used for closed-loop, and runs the artefact cancellation and closed-loop algorithms. It connects to a 2 Mb s^{-1} 2.4 GHz low-energy radio (nRF51822; Nordic Semiconductor) via a serial peripheral interface running at 3.08 MHz to form a bidirectional, half-duplex link with the base station and GUI.

We developed a radio protocol using a time division duplex scheme, allowing low-bitrate commands to be sent from the base station to the board, and high-bitrate neural recordings to be continuously streamed out for logging. The exact division between uplink and downlink can be adjusted to suit the application and streaming state, with a maximum effective bitrate of ~1.6 Mb s^{-1}. Two streaming modes are available. In the open-loop mode, 96 channels of data are streamed to the base station. In the closed-loop mode, only the control channel

and one of the stimulation channels are streamed, along with the calculated power spectral density.

A 20 MHz crystal oscillator provides a clock source to the FPGA and processor, which then generates a 20.48 MHz clock for the NMICs (Cortera Neurotechnologies). On-board buck converters (TPS6226x; Texas Instruments) generate the 1.2, 1.8, 2.5 and 3 V supplies needed by the rest of the system from a pair of 4.1 V, 250 mAh lithium-ion batteries (ICP521630; Renata). A battery charger integrated circuit (LTC4065; Linear Technology) and three-way connector allow for the battery to be safely charged without disconnecting it from the system.

A 6-axis accelerometer and gyroscope (MPU-6050; InvenSense) and 512 Mb low-power synchronous dynamic random access memory (MT46H32M16LFBF-5; Micron Technology) are also connected to the processor through an inter-integrated circuit (I^2C) and double data rate bus, respectively, although these were not used in this work.

Device fabrication steps consisted of fabricating the eight-layer printed circuit board (PCB), populating board components, wire-bonding the NMICs and soldering the neuro nano-strip connectors (custom order; Omnetics Connector) for interfacing with the microdrive electrode array. FPGA hardware was written in Verilog, while the Cortex-M3 and radio were programmed in C. A combined Joint Test Action Group and Serial Wire Debug connector allows users to reprogramme and debug SmartFusion2 and radio.

Base station and software GUI. A wireless base station consisting of a radio (nRF51822 Evaluation Kit; Nordic Semiconductor) and a serial peripheral interface–universal serial bus bridge (CP2130EK; Silicon Labs) was used to communicate with WAND (Fig. 1d). A custom-built Python GUI was developed to control and monitor data streamed from WAND on a PC (Supplementary Fig. 5). Users can set up the system for multiple use cases, visualize real-time neural recordings, configure all NMIC settings and configure the closed-loop classification algorithm. Recorded data are saved in HDF5 data format, along with relevant-use case settings, NMIC configurations and other notes for the recording.

NMICs (Cortera Neurotechnologies). The recording subsystem on each NMIC (Fig. 1c and Supplementary Fig. 3) comprises 64 mixed-signal 15-bit recording channels operating at 1,000 samples s^{-1}. Each recording channel has a selectable input voltage range of 100 or 400 mV, allowing simultaneous amplification and digitization of the electrode offset, neural signal and stimulation artefact within the linear range.

The four on-chip stimulators can be multiplexed to any of the electrodes and allow for a variety of programmable stimulation parameters, including current amplitudes, pulse timing and frequencies (Supplementary Fig. 1). Stimulation pulses are delivered in three phases: a set-up phase with configurable set-up time; a pulse phase configurable to be mono- or biphasic with configurable pulse widths and interphase gap; and a shorting phase with a configurable shorting time where electrodes are shorted to the reference. The NMIC assists in artefact cancellation by flagging all samples coinciding with any of the stimulators being active; however, samples coinciding with the shorting phase only are not flagged and care must be taken to also remove artefacts from those samples (Fig. 5b). The artefact flag is implemented as a single bit appended after the most significant bit of the 15-bit ADC value, creating a 16-bit value per sample per channel. To enable low-latency (sub-ms), highly programmable stimulation (225 bits of customization), the NMIC uses double-content shadow registers, meaning stimulation parameters can be changed while the previous stimulation pulse or waveform is executed. A low-overhead command initiates a programmed stimulation pattern.

On-chip programmable d.c.–d.c. converters provide a 1 V supply to the recording and digital circuits, as well as a selectable 3, 6, 9 or 12 V supply to the stimulator, adjusting the compliance for different stimulation regimes for improved power efficiency (Supplementary Fig. 3). All power management is therefore integrated on the chip, enabling power from a single supply without the need for large off-chip power conversion circuits[26].

Artefact cancellation and open-loop experiment analysis. Frames of concurrent 16-bit samples from the enabled NMIC recording channels arrive at the FPGA every 1 ms. Because some unflagged samples may still be affected by the shorting phase, our artefact cancellation always interpolates over the maximum number of consecutive flagged samples possible after detection of the first artefact sample (Fig. 5b). This can be calculated by finding the length (in ms) of the entire pulse, rounding it up to the nearest integer and adding 1. For biphasic 125 µs pulses with a 31.25 µs interphase gap and 31.25 µs shorting phase, the length of the pulse is 0.3125 ms, which requires 2 samples to be cancelled per artefact.

Artefact cancellation is implemented on the ARM Cortex-M3 processor before packetization of data for wireless transmission or use in the closed-loop algorithm. Eight frames of samples are buffered, allowing cancellation of artefacts lasting up to seven frames. Artefacts are detected upon finding the first frame with a set artefact flag, and cancelled once the first clean frame is received. Because of the 8-frame buffering, there is a delay of 8 ms between frames being received by the FPGA and frames being transmitted to the base station or being used for the closed-loop algorithm.

Closed-loop algorithm. The closed-loop control algorithm is implemented in the ARM Cortex-M3 processor and triggers stimulation based on real-time spectral analysis of any of the 128 recording channels (Fig. 6a,b). We compute the power spectrum of buffered windows of data using the fixed-point fast Fourier transform and magnitude squared functions of the ARM Cortex Microcontroller Software Interface Standard digital signal processing library. Each window is demeaned and scaled 64 times before computation. The window length, N, can be configured from the GUI to be any power of 2 between 16 and 2,048, and successive windows overlap by $N/2$ samples.

From the power spectrums, we can derive up to two control signals. Each control signal can either be the integrated power across a specified frequency band or the derivative of that power estimated by subtracting the newly calculated power value from the previous one. For each control signal, we can specify the threshold for either the power or derivative. After each calculation, the decision to stimulate can either be the logical AND or logical OR of the threshold crossings from each control signal. A programmable 'dead time' can be applied to prevent stimulation being triggered by consecutive power measurements. An additional random control mode triggers stimulation pulse trains at pseudorandom intervals between configurable minimum and maximum time intervals.

Surgery and electrophysiology. A customized semichronic microelectrode array (Gray Matter Research) was implanted unilaterally in one male rhesus macaque (*Macaca mulatta*; weight ~9.1 kg; age 9 years) (Fig. 1a–d). The subject was implanted unilaterally with the custom-machined chamber, enabling access to premotor and motor cortical regions. The chamber position was calculated based on images obtained from 1.5 T MRI scans of the subject's brain. The semichronic array features a titanium chamber form-fitted to the cranium of the subject and a microdrive housing 157 single microelectrodes that are independently moveable in the depth axis. The microdrive sits within the implanted chamber and a sterile seal for the system is maintained. The microelectrodes are gradually lowered into neural tissue over time and their positions are adjusted throughout the experiment to better isolate neural activity in the nuclei of interest. Electrode positions are controlled by miniature-screw-driven actuators travelling along threaded rods. Electrical contact with the electrodes is achieved through a PCB, and Omnetics headers are used to connect the PCB to neural recording systems, such as WAND or standard tethered electrophysiology equipment. Two types of microelectrodes were used in the semichronic array. The first were tungsten electrodes with epoxylite insulation (500–800 kOhm; FHC)—a standard electrode type for acute neural recording experiments. The second were platinum–iridium (PtIr) electrodes with parylene-C insulation, which are standard for neuromodulation experiments (200–350 kOhm; Microprobes; Alpha Omega). Electrical stimulation in this study was exclusively performed using the PtIr microelectrodes. All experiments were performed in compliance with the National Institutes of Health Guide for the Care and Use of Laboratory Animals, and were approved by the University of California, Berkeley Institutional Animal Care and Use Committee (protocol AUP-2014–09–6720).

Primate experimental procedures. Overnight recordings were carried out with the subject moving freely throughout the home environment, and were typically taken from approximately 20:00 to 06:00 (Fig. 4a). The subject was pair-housed with an NHP cagemate and was in social contact with the cagemate throughout the recording session. It is worth noting that the dimensions of the home-cage environment could accommodate up to four NHPs, and thus it is feasible to utilize WAND for recording from a small population of socially housed animals without compromising the streaming wireless signal integrity. The base station receiver was mounted on the ceiling approximately 0.5 m from the top of the cage and was connected to a computer running the custom-built GUI application for acquiring the neural recordings.

The subject was also trained in a standard centre-out joystick task and a delayed-reach joystick task for in-chair behavioural recordings and for the closed-loop experiment (Figs. 3a and 6b). Both tasks were self-paced. Briefly, the subject was trained to use a joystick to control a cursor on a computer screen and move to circular targets presented on the screen. The joystick was affixed to the front of the primate chair and the subject was free to use either hand at any point in the task to control the joystick.

In the centre-out task (Fig. 3a), a trial begins with the subject holding the cursor at a centre circular target for 500 ms. Following this hold period, a peripheral target appears at one of eight target locations equally distributed around the centre target at a distance of 10 cm, and the centre target is removed from the screen, acting as a 'go cue'. The subject then moves the cursor (that is, 'reaches') to the peripheral target and holds at this target for another 500 ms. If successful, the subject is administered a small juice reward lasting 800–1,000 ms. A trial was considered successful if the subject completed the two hold periods within a 10 s period.

The sequence of events in the delayed-reach joystick task (Fig. 6b) is similar to the centre-out task, with the exception being that the peripheral target appears before the 'go cue', which is signalled with the disappearance of the centre target. The hold period for the centre target lasts 400 ms before the peripheral target is shown. This initiates the 'delay period', the duration of which varied randomly

trial by trial with a range of 200–400 ms. After the delay period, the centre target disappears from the screen, signalling the 'go cue', and the subject is cued to reach to the peripheral target. The range of delay durations was chosen to allow for movement preparation and to ensure that microstimulation occurred near the go cue for a non-trivial number of trials.

Open-loop artefact cancellation experiment. The open-loop artefact cancellation experiments consisted of continuous recordings made with 30 s of no stimulation, 30 s of stimulation with no artefact cancellation and 30 s of stimulation with artefact cancellation for each set of stimulation parameters. Biphasic stimulation, with amplitudes swept in 40 µA steps between 40 and 160 µA, were delivered for pulse widths of 125 and 62.5 µs and with 100 and 20 Hz stimulation frequencies. Stimulation electrodes were chosen to be the same as for the closed-loop experiment. During the open-loop stimulation experiments, the monkey was in-chair and did not perform any tasks.

Artefacts recorded with back-end cancellation disabled were sorted offline into ten-sample windows aligned with sample 0 as the clean sample before the artefact started and sample 1 as the first flagged sample of the artefact (Fig. 5c). These segments were used to analyse the size and consistency of recorded artefacts. Offsets were then subtracted from each window such that sample 0 was 0 V. Artefact amplitude was calculated as the average sum of the magnitudes of samples 1 and 2. Artefact duration was then calculated as the average number of samples for which the magnitude was greater than −60 dB of the maximum calculated artefact amplitude.

To determine the effectiveness of cancellation, the power spectrum for each epoch of stimulation and artefact cancellation was estimated using Welch's averaged modified periodogram method with 1,000 Hanning windowed samples and overlaps of 500 samples.

Closed-loop experiment. For the closed-loop experiment, we used a window length of $N = 512$ to calculate the beta power (13–30 Hz) and the derivative of beta power as our control signals. Stimulation was enabled when the beta power exceeded 33 μV_{rms} and the delta of the beta power exceeded 10.45 μV_{rms}. The dead time was set to 3 power-calculation windows, or 768 ms (Fig. 6b). Biphasic, bipolar stimulation was delivered to PtIr electrodes 52 and 53 in PMd. Stimulation pulses were 160 µA in amplitude with 125 µs pulse widths and a 31.25 µs shorting phase. Pulse trains were 18 pulses long and delivered at 256 Hz.

Reaction time was defined as the length of time following the go cue for the cursor speed to first achieve a threshold of 5 cm s^{-1}. Reaction times below 50 ms were discarded as they were probably due to the subject initiating movement before the go cue, and reaction times above 1 s were also not considered as they indicate a low level of engagement in the task.

Study approval. All experiments were performed in compliance with the National Institutes of Health Guide for the Care and Use of Laboratory Animals and were approved by the University of California, Berkeley Institutional Animal Care and Use Committee (protocol AUP-2014–09–6720).

Reporting Summary. Further information on research design is available in the Nature Research Reporting Summary linked to this article.

Code availability. The codes used for this study are available on GitHub at https://github.com/MullerGroup/WAND.

Data availability

The data that support the findings of this study are available from the corresponding author upon reasonable request.

Received: 4 December 2017; Accepted: 30 October 2018;
Published online: 31 December 2018

References

1. Eisenstein, M. Electrotherapy: shock value. *Nature* **538**, S10–S12 (2016).
2. Sun, F. T. & Morrell, M. J. Closed-loop neurostimulation: the clinical experience. *Neurotherapeutics* **11**, 553–563 (2014).
3. Sun, F. T., Morrell, M. J. & Wharen, R. E. Responsive cortical stimulation for the treatment of epilepsy. *Neurotherapeutics* **5**, 68–74 (2008).
4. Rosin, B. et al. Closed-loop deep brain stimulation is superior in ameliorating parkinsonism. *Neuron* **72**, 370–384 (2011).
5. Little, S. et al. Adaptive deep brain stimulation in advanced Parkinson disease. *Ann. Neurol.* **74**, 449–457 (2013).
6. Morrell, M. J. Responsive cortical stimulation for the treatment of medically intractable partial epilepsy. *Neurology* **77**, 1295–1304 (2011).
7. Beuter, A., Lefaucheur, J.-P. & Modolo, J. Closed-loop cortical neuromodulation in Parkinson's disease: an alternative to deep brain stimulation? *Clin. Neurophysiol.* **125**, 874–885 (2014).
8. Swann, N. C. et al. Gamma oscillations in the hyperkinetic state detected with chronic human brain recordings in Parkinson's disease. *J. Neurosci.* **36**, 6445–6458 (2016).
9. Little, S. et al. Bilateral adaptive deep brain stimulation is effective in Parkinson's disease. *J. Neurol. Neurosurg. Psychiatry* **87**, 717–721 (2016).
10. Malekmohammadi, M. et al. Kinematic adaptive deep brain stimulation for resting tremor in Parkinson's disease. *Mov. Disord.* **31**, 426–428 (2016).
11. Rosa, M. et al. Adaptive deep brain stimulation in a freely moving parkinsonian patient. *Mov. Disord.* **30**, 1003–1005 (2015).
12. Yin, M. et al. Wireless neurosensor for full-spectrum electrophysiology recordings during free behavior. *Neuron* **84**, 1170–1182 (2014).
13. Gao, H. et al. HermesE: a 96-channel full data rate direct neural interface in 0.13 µm CMOS. *IEEE J. Solid-State Circuits* **47**, 1043–1055 (2012).
14. Stanslaski, S. et al. Design and validation of a fully implantable, chronic, closed-loop neuromodulation device with concurrent sensing and stimulation. *IEEE. Trans. Neural Syst. Rehabil. Eng.* **20**, 410–421 (2012).
15. Zanos, S., Richardson, A. G., Shupe, L., Miles, F. P. & Fetz, E. E. The neurochip-2: an autonomous head-fixed computer for recording and stimulating in freely behaving monkeys. *IEEE. Trans. Neural Syst. Rehabil. Eng.* **19**, 427–435 (2011).
16. Liu, X. et al. The PennBMBI: a general purpose wireless brain–machine–brain interface system for unrestrained animals. In *2014 IEEE International Symposium on Circuits and Systems* 650–653 (IEEE, 2014).
17. *RNS System User Manual* (NeuroPace, 2015).
18. Bagheri, A. et al. Massively-parallel neuromonitoring and neurostimulation rodent headset with nanotextured flexible microelectrodes. *IEEE Trans. Biomed. Circuits Syst.* **7**, 601–609 (2013).
19. Kassiri, H. et al. Closed-loop neurostimulators: a survey and a seizure-predicting design example for intractable epilepsy treatment. *IEEE Trans. Biomed. Circuits Syst.* **11**, 1026–1040 (2017).
20. Abdelhalim, K., Jafari, H. M., Kokarovtseva, L., Velazquez, J. L. P. & Genov, R. 64-Channel UWB wireless neural vector analyzer SOC with a closed-loop phase synchrony-triggered neurostimulator. *IEEE J. Solid-State Circuits* **48**, 2494–2510 (2013).
21. Kassiri, H. et al. Rail-to-rail-input dual-radio 64-channel closed-loop neurostimulator. *IEEE J. Solid-State Circuits* **52**, 2793–2810 (2017).
22. Cheng, C.-H. et al. A fully integrated closed-loop neuromodulation SoC with wireless power and bi-directional data telemetry for real-time human epileptic seizure control. In *Symposium on VLSI Circuits* C44–C45 (IEEE, 2017).
23. Kassiri, H. et al. Battery-less tri-band-radio neuro-monitor and responsive neurostimulator for diagnostics and treatment of neurological disorders. *IEEE J. Solid-State Circuits* **51**, 1274–1289 (2016).
24. Rhew, H. G. et al. A fully self-contained logarithmic closed-loop deep brain stimulation SoC with wireless telemetry and wireless power management. *IEEE J. Solid-State Circuits* **49**, 2213–2227 (2014).
25. Chen, W. M. et al. A fully integrated 8-channel closed-loop neural-prosthetic CMOS SoC for real-time epileptic seizure control. *IEEE J. Solid-State Circuits* **49**, 232–247 (2014).
26. Johnson, B. C. et al. An implantable 700 µW 64-channel neuromodulation IC for simultaneous recording and stimulation with rapid artifact recovery. In *Symposium on VLSI Circuits* C48–C49 (IEEE, 2017).
27. Kuhn, A. A. et al. High-frequency stimulation of the subthalamic nucleus suppresses oscillatory activity in patients with Parkinson's disease in parallel with improvement in motor performance. *J. Neurosci.* **28**, 6165–6173 (2008).
28. Yoshida, F. et al. Value of subthalamic nucleus local field potentials recordings in predicting stimulation parameters for deep brain stimulation in Parkinson's disease. *J. Neurol. Neurosurg. Psychiatry* **81**, 885–889 (2010).
29. Weinberger, M. et al. Beta oscillatory activity in the subthalamic nucleus and its relation to dopaminergic response in Parkinson's disease. *J. Neurophysiol.* **96**, 3248–3256 (2006).
30. Halpern, C. H., Samadani, U., Litt, B., Jaggi, J. L. & Baltuch, G. H. Deep brain stimulation for epilepsy. *Neurotherapeutics* **5**, 59–67 (2008).
31. So, K., Dangi, S., Orsborn, A. L., Gastpar, M. C. & Carmena, J. M. Subject-specific modulation of local field potential spectral power during brain–machine interface control in primates. *J. Neural Eng.* **11**, 26002 (2014).
32. Flint, R. D., Lindberg, E. W., Jordan, L. R., Miller, L. E. & Slutzky, M. W. Accurate decoding of reaching movements from field potentials in the absence of spikes. *J. Neural Eng.* **9**, 46006 (2012).
33. Flint, R. D., Ethier, C., Oby, E. R., Miller, L. E. & Slutzky, M. W. Local field potentials allow accurate decoding of muscle activity. *J. Neurophysiol.* **108**, 18–24 (2012).
34. Khanna, P. & Carmena, J. M. Beta band oscillations in motor cortex reflect neural population signals that delay movement onset. *eLife* **6**, 1–31 (2017).
35. Stavisky, S. D., Kao, J. C., Nuyujukian, P., Ryu, S. I. & Shenoy, K. V. A high performing brain–machine interface driven by low-frequency local field potentials alone and together with spikes. *J. Neural Eng.* **12**, 36009 (2015).
36. Rubino, D., Robbins, K. A. & Hatsopoulos, N. G. Propagating waves mediate information transfer in the motor cortex. *Nat. Neurosci.* **9**, 1549–1557 (2006).
37. Sanes, J. N. & Donoghue, J. P. Oscillations in local field potentials of the primate motor cortex during voluntary movement. *Proc. Natl Acad. Sci. USA* **90**, 4470–4474 (1993).

38. Mehring, C. et al. Inference of hand movements from local field potentials in monkey motor cortex. *Nat. Neurosci.* **6**, 1253–1254 (2003).
39. Leventhal, D. K. et al. Basal ganglia beta oscillations accompany cue utilization. *Neuron* **73**, 523–536 (2012).
40. Lundqvist, M. et al. Gamma and beta bursts underlie working memory. *Neuron* **90**, 152–164 (2016).
41. Pesaran, B. et al. Temporal structure in neuronal activity during working memory in macaque parietal cortex. *Nat. Neurosci.* **5**, 805–811 (2002).
42. Harrison, R. R. et al. A low-power integrated circuit for a wireless 100-electrode neural recording system. *IEEE J. Solid-State Circuits* **42**, 123–133 (2007).
43. Zhang, Fan, Holleman, J. & Otis, B. P. Design of ultra-low power biopotential amplifiers for biosignal acquisition applications. *IEEE Trans. Biomed. Circuits Syst.* **6**, 344–355 (2012).
44. Shulyzki, R. et al. 320-Channel active probe for high-resolution neuromonitoring and responsive neurostimulation. *IEEE Trans. Biomed. Circuits Syst.* **9**, 34–49 (2015).
45. Liu, X., Zhang, M., Richardson, A. G., Lucas, T. H. & Van der Spiegel, J. Design of a closed-loop, bidirectional brain machine interface system with energy efficient neural feature extraction and PID control. *IEEE Trans. Biomed. Circuits Syst.* **11**, 729–742 (2017).
46. Jiang, W., Hokhikyan, V., Chandrakumar, H., Karkare, V. & Marković, D. A ±50-mV linear-input-range VCO-based neural-recording front-end with digital nonlinearity correction. *IEEE J. Solid-State Circuits* **52**, 173–184 (2017).
47. Mendrela, A. E. et al. A bidirectional neural interface circuit with active stimulation artifact cancellation and cross-channel common-mode noise suppression. *IEEE J. Solid-State Circuits* **51**, 955–965 (2016).
48. Culaclii, S., Kim, B., Lo, Y.-K. & Liu, W. A hybrid hardware and software approach for cancelling stimulus artifacts during same-electrode neural stimulation and recording. In *38th Annual International Conference of the IEEE Engineering in Medicine and Biology Society* 6190–6193 (IEEE, 2016).
49. Heer, F. et al. Single-chip microelectronic system to interface with living cells. *Biosens. Bioelectron.* **22**, 2546–2553 (2007).
50. Viswam, V. et al. 2048 action potential recording channels with 2.4 μVrms noise and stimulation artifact suppression. In *IEEE Biomedical Circuits and Systems Conference* 136–139 (IEEE, 2016).
51. Limnuson, K., Lu, H., Chiel, H. J. & Mohseni, P. Real-time stimulus artifact rejection via template subtraction. *IEEE Trans. Biomed. Circuits Syst.* **8**, 391–400 (2014).
52. Wichmann, T. & Devergnas, A. A novel device to suppress electrical stimulus artifacts in electrophysiological experiments. *J. Neurosci. Methods* **201**, 1–8 (2011).
53. Heffer, L. F. & Fallon, J. B. A novel stimulus artifact removal technique for high-rate electrical stimulation. *J. Neurosci. Methods* **170**, 277–284 (2008).
54. Hoffmann, U., Cho, W., Ramos-Murguialday, A. & Keller, T. Detection and removal of stimulation artifacts in electroencephalogram recordings. In *Proc. Annual International Conference of the IEEE Engineering in Medicine and Biology Society* 7159–7162 (IEEE, 2011).
55. Waddell, C., Pratt, J. A., Porr, B. & Ewing, S. Deep brain stimulation artifact removal through under-sampling and cubic-spline interpolation. In *2nd International Congress on Image and Signal Processing* 1–5 (IEEE, 2009).
56. Dadarlat, M. C., O'Doherty, J. E. & Sabes, P. N. A learning-based approach to artificial sensory feedback leads to optimal integration. *Nat. Neurosci.* **18**, 138–144 (2014).
57. Pais-Vieira, M., Lebedev, M., Kunicki, C., Wang, J. & Nicolelis, M. A. L. A brain-to-brain interface for real-time sharing of sensorimotor information. *Sci. Rep.* **3**, 1–10 (2013).
58. Fitzsimmons, N. A., Drake, W., Hanson, T. L., Lebedev, M. A. & Nicolelis, M. A. L. Primate reaching cued by multichannel spatiotemporal cortical microstimulation. *J. Neurosci.* **27**, 5593–5602 (2007).
59. O'Doherty, J. E. et al. Active tactile exploration using a brain–machine–brain interface. *Nature* **479**, 228–231 (2011).
60. O'Doherty, J. E., Lebedev, M. A., Li, Z. & Nicolelis, M. A. L. Virtual active touch using randomly patterned intracortical microstimulation. *IEEE. Trans. Neural Syst. Rehabil. Eng.* **20**, 85–93 (2012).
61. Zaaimi, B., Ruiz-Torres, R., Solla, S. A. & Miller, L. E. Multi-electrode stimulation in somatosensory cortex increases probability of detection. *J. Neural Eng.* **10**, 56013 (2013).
62. Moin, A. et al. Powering and communication for OMNI: a distributed and modular closed-loop neuromodulation device. In *38th Annual International Conference of the IEEE Engineering in Medicine and Biology Society* 4471–4474 (IEEE, 2016).
63. Canolty, R. T., Ganguly, K. & Carmena, J. M. Task-dependent changes in cross-level coupling between single neurons and oscillatory activity in multiscale networks. *PLoS Comput. Biol.* **8**, e1002809 (2012).
64. Saleh, M., Reimer, J., Penn, R., Ojakangas, C. L. & Hatsopoulos, N. G. Clinical study fast and slow oscillations in human primary motor cortex predict oncoming behaviorally relevant cues. *Neuron* **65**, 461–471 (2010).
65. Bastian, A., Schoner, G. & Riehle, A. Preshaping and continuous evolution of motor cortical representations during movement preparation. *Eur. J. Neurosci.* **18**, 2047–2058 (2003).
66. Churchland, M. M., Yu, B. M., Ryu, S. I., Santhanam, G. & Shenoy, K. V. Neural variability in premotor cortex provides a signature of motor preparation. *J. Neurosci.* **26**, 3697–3712 (2006).
67. Churchland, M. M. & Shenoy, K. V. Delay of movement caused by disruption of cortical preparatory activity. *J. Neurophysiol.* **97**, 348–359 (2007).
68. Donoghue, J. P., Sanes, J. N., Hatsopoulos, N. G. & Gaal, G. Neural discharge and local field potential oscillations in primate motor cortex during voluntary movements. *J. Neurophysiol.* **79**, 159–173 (1998).
69. Cantero, J. L., Atienza, M. & Salas, R. M. Human alpha oscillations in wakefulness, drowsiness period, and REM sleep: different electroencephalographic phenomena within the alpha band. *Neurphysiol. Clin.* **32**, 54–71 (2002).
70. Schulz, H. Rethinking sleep analysis. *J. Clin. Sleep Med.* **4**, 99–103 (2008).
71. Rouse, A. G. et al. A chronic generalized bi-directional brain–machine interface. *J. Neural Eng.* **8**, 36018 (2011).
72. Avestruz, A.-T. et al. A 5 μW/channel spectral analysis IC for chronic bidirectional brain–machine interfaces. *IEEE J. Solid-State Circuits* **43**, 3006–3024 (2008).
73. Salam, M. T., Perez Velazquez, J. L. & Genov, R. Seizure suppression efficacy of closed-loop versus open-loop deep brain stimulation in a rodent model of epilepsy. *IEEE. Trans. Neural Syst. Rehabil. Eng.* **24**, 710–719 (2016).
74. Public-Private Partnership Program: devices and support specific manufacturers. *NIH BRAIN Initiative* https://www.braininitiative.nih.gov/resources/public-private-partnership-program-devices-support-specific-manufacturers (2018).
75. Thomas, G. P. & Jobst, B. C. Critical review of the responsive neurostimulator system for epilepsy. *Med. Devices* **8**, 405–411 (2015).
76. Lempka, S. F., Howell, B., Gunalan, K., Machado, A. G. & McIntyre, C. C. Characterization of the stimulus waveforms generated by implantable pulse generators for deep brain stimulation. *Clin. Neurophysiol.* **129**, 731–742 (2018).

Acknowledgements

This work was supported in part by the Defense Advanced Research Projects Agency (W911NF-14–2–0043 to R.M., J.M.R. and J.M.C.) and National Science Foundation Graduate Research Fellowship Program (grant number 1106400 to A.Z.). The authors thank the Wagner Foundation and the sponsors of the Berkeley Wireless Research Center. They also thank E. Alon, S. Gambini and I. Izyumin for technical discussion.

Author contributions

J.M.R., J.M.C and R.M. are co-principal investigators. A.Z., B.C.J., G.A., A.M., F.L.B., J.M.R. and R.M. designed and tested the system. B.C.J. and R.M. designed and tested the integrated circuits. S.R.S. and J.M.C. designed the in vivo experiments. A.Z., S.R.S., B.C.J., G.A. and A.M. performed the experiments and analysis. J.M.R., J.M.C. and R.M. oversaw the project. A.Z., S.R.S., B.C.J., G.A., A.M., J.M.R., J.M.C. and R.M. wrote and edited the paper.

Competing interests

B.C.J., J.M.R., J.M.C. and R.M. have financial interests in Cortera Neurotechnologies, which has filed a patent application on the integrated circuit used in this work.

Additional information

Supplementary information is available for this paper at https://doi.org/10.1038/s41551-018-0323-x.

Reprints and permissions information is available at www.nature.com/reprints.

Correspondence and requests for materials should be addressed to R.M.

Publisher's note: Springer Nature remains neutral with regard to jurisdictional claims in published maps and institutional affiliations.

nature research

Corresponding author(s): Rikky Muller

Reporting Summary

Nature Research wishes to improve the reproducibility of the work that we publish. This form provides structure for consistency and transparency in reporting. For further information on Nature Research policies, see Authors & Referees and the Editorial Policy Checklist.

Statistical parameters

When statistical analyses are reported, confirm that the following items are present in the relevant location (e.g. figure legend, table legend, main text, or Methods section).

n/a	Confirmed	
☐	☒	The exact sample size (*n*) for each experimental group/condition, given as a discrete number and unit of measurement
☐	☒	An indication of whether measurements were taken from distinct samples or whether the same sample was measured repeatedly
☐	☒	The statistical test(s) used AND whether they are one- or two-sided *Only common tests should be described solely by name; describe more complex techniques in the Methods section.*
☒	☐	A description of all covariates tested
☒	☐	A description of any assumptions or corrections, such as tests of normality and adjustment for multiple comparisons
☐	☒	A full description of the statistics including central tendency (e.g. means) or other basic estimates (e.g. regression coefficient) AND variation (e.g. standard deviation) or associated estimates of uncertainty (e.g. confidence intervals)
☐	☒	For null hypothesis testing, the test statistic (e.g. *F*, *t*, *r*) with confidence intervals, effect sizes, degrees of freedom and *P* value noted *Give P values as exact values whenever suitable.*
☒	☐	For Bayesian analysis, information on the choice of priors and Markov chain Monte Carlo settings
☒	☐	For hierarchical and complex designs, identification of the appropriate level for tests and full reporting of outcomes
☐	☒	Estimates of effect sizes (e.g. Cohen's *d*, Pearson's *r*), indicating how they were calculated
☐	☒	Clearly defined error bars *State explicitly what error bars represent (e.g. SD, SE, CI)*

Our web collection on statistics for biologists may be useful.

Software and code

Policy information about availability of computer code

Data collection	See Methods sections 'WAND board components' and 'Base station and software GUI'.
Data analysis	Data were analysed using Matlab (Mathworks, Inc.) and Python.

For manuscripts utilizing custom algorithms or software that are central to the research but not yet described in published literature, software must be made available to editors/reviewers upon request. We strongly encourage code deposition in a community repository (e.g. GitHub). See the Nature Research guidelines for submitting code & software for further information.

Data

Policy information about availability of data

All manuscripts must include a data availability statement. This statement should provide the following information, where applicable:

- Accession codes, unique identifiers, or web links for publicly available datasets
- A list of figures that have associated raw data
- A description of any restrictions on data availability

The data that support the findings of this study are available from the corresponding author upon reasonable request.

Field-specific reporting

Please select the best fit for your research. If you are not sure, read the appropriate sections before making your selection.

☒ Life sciences ☐ Behavioural & social sciences ☐ Ecological, evolutionary & environmental sciences

For a reference copy of the document with all sections, see nature.com/authors/policies/ReportingSummary-flat.pdf

Life sciences study design

All studies must disclose on these points even when the disclosure is negative.

Sample size	The study was carried out with a single animal subject. Animal experiments for this study were intended to demonstrate device capabilities rather than the effect of neuromodulation therapies on animal subjects. Thus, multiple repeated experiments on a single animal subject were sufficient.
Data exclusions	No data were excluded from the analyses.
Replication	All attempts at experimental replication were successful.
Randomization	Randomization was not relevant (single subject).
Blinding	Blinding was not relevant to our experiments, as there were no subjective elements to the assessment of the device's capabilities.

Reporting for specific materials, systems and methods

Materials & experimental systems

n/a	Involved in the study
☒	☐ Unique biological materials
☒	☐ Antibodies
☒	☐ Eukaryotic cell lines
☒	☐ Palaeontology
☐	☒ Animals and other organisms
☒	☐ Human research participants

Methods

n/a	Involved in the study
☒	☐ ChIP-seq
☒	☐ Flow cytometry
☒	☐ MRI-based neuroimaging

Animals and other organisms

Policy information about studies involving animals; ARRIVE guidelines recommended for reporting animal research

Laboratory animals	One male rhesus macaque (Macaca mulatta, weight ~9.1 kg, age 9 years).
Wild animals	This study did not involve wild animals.
Field-collected samples	This study did not involve field-collected samples.